

Numerical simulation of multicomponent flows with the presence of density gradients for the upgrading of advanced turbulence models

Huang, M.; Höhne, T.;

Originally published:

April 2019

Nuclear Engineering and Design 344(2019), 28-37

DOI: <https://doi.org/10.1016/j.nucengdes.2019.01.025>

Perma-Link to Publication Repository of HZDR:

<https://www.hzdr.de/publications/Publ-28760>

Release of the secondary publication
on the basis of the German Copyright Law § 38 Section 4.

CC BY-NC-ND

Numerical simulation of multicomponent flows with the presence of density gradients for the upgrading of advanced turbulence models

M. Huang, T. Höhne

¹Helmholtz-Zentrum Dresden-Rossendorf (HZDR) - Institute of Fluid Dynamics
Bautzner Landstraße 400, D-01328 Dresden, Germany

Abstract

The turbulence effects during the buoyancy-driven mixing was investigated at a vertical mixing (VeMix) test facility, which was developed to investigate the mixing of high borated and low borated coolant in nuclear reactor. Additional buoyancy terms are included in buoyancy-modified turbulence models, which have been implemented in the CFD code ANSYS CFX and validated with experimental data captured by optical methods and conductivity measurement technology. The physicality of the flow phenomena and the vortical oscillations analyzed by Fourier transformation in both the experiments and simulations show good agreement under different flow conditions. The influence of different buoyancy models were investigated in detail and optimal models for simulations at similar flow conditions have been selected.

KEYWORDS

Multicomponent flow, CFD, turbulence models, SBES, RANS, LES

1. Introduction

During the operation of a nuclear reactor, the reactivity of the reactor core should be controlled through the use of control rods or neutron absorbers dissolved in the coolant. In pressurized water reactors (PWRs), boron is commonly used as the neutron absorber and the cooling of the reactor core with boron-moderated water is therefore a critical issue with respect to the reactivity of the reactor core. In certain accident scenarios such as boron dilution issues, turbulent mixing between high borated and low borated coolant may occur and buoyancy forces due to density differences may influence the mixing process significantly [7]. Such buoyancy-affected coolant

mixing in the reactor pressure vessel has been in the scope of investigations in recent years [3,7,8,9]. However, as nuclear reactor geometries are complex and require great efforts in experimental and numerical investigations, simpler models should be developed to provide a basic understanding of the buoyancy-affected mixing from a more general point of view. For this purpose, a simple vertical mixing test facility (VeMix) was constructed at the Helmholtz-Zentrum Dresden-Rossendorf (HZDR). Optical and surface wire mesh measurements at the VeMix facility were conducted by Da Silva et al. [18,19] to qualitatively and quantitatively investigate the mixing process. Corresponding numerical simulations were performed by Vaibar [21,22] in 2007 to validate the CFD codes existing at that time.

Considering the increased computing power and the developments in turbulence modelling in recent years [5], the turbulent mixing in the VeMix test facility was reinvestigated with a comprehensive range of turbulence models in the current study. Reynolds-Averaged Navier-Stokes (RANS) model, i.e., the Shear Stress Transport (SST) model [12], as well as Scale-Resolving Simulation (SRS) models including Large Eddy Simulation (LES) [20], Scale-Adaptive Simulation (SAS) [15] and Stress-Blended Eddy Simulation (SBES) [14] for calculating flows with strong density gradients were validated with experimental data in Da Silva et al. [18,19].

In RANS-based models, commercial CFD code usually treats buoyancy effects within the isotropic eddy-diffusivity hypothesis [1], while buoyancy induces anisotropy. Therefore, higher order turbulence models [2,6] have been developed, implemented and validated which take into account that anisotropy. In LES, the buoyancy effects were directly resolved for the large eddies, but not modelled in the subgrid-scale (SGS) models in present CFX code. In order to evaluate the buoyancy effects on the unresolved smaller scales, additional buoyancy production terms proposed in Eidson [4] and in Peng & Davidson [16] were slightly adapted and implemented into the Smagorinsky model in CFX. These buoyancy-modified turbulence models were validated with the experimental data, in order to find an optimal model for the simulation of the fluid mixing under similar flow conditions. Focused on the improved simulation of the buoyancy driven mixing process, this work contributes to the validation of turbulence models under influence of buoyancy forces and therefore

to the enhancement of the prediction accuracy of boron concentration in nuclear reactors, which is relevant to the analysis of the nuclear reactor safety.

2. Experimental setup

The VeMix test facility is a simple upright channel of a rectangular cross section and is set up to ensure that the gravity force acts along the significant length scale, the channel height. Figure 1 shows the design of the VeMix test facility which consists of five identical rectangular segments. Each segment is 500 mm wide, 625 mm high, 100 mm deep, and is made of acrylic glass to allow optical measurements. An inlet nozzle is located between segments 1 and 2, while an outlet nozzle is positioned between segments 4 and 5. Pure deionized water was used as the light fluid and a 6% water-sucrose mixture is used as the heavy fluid. The latter has a density of 1020 kg/m³, i.e. 2% density difference ($\Delta\rho$) compared to pure water.

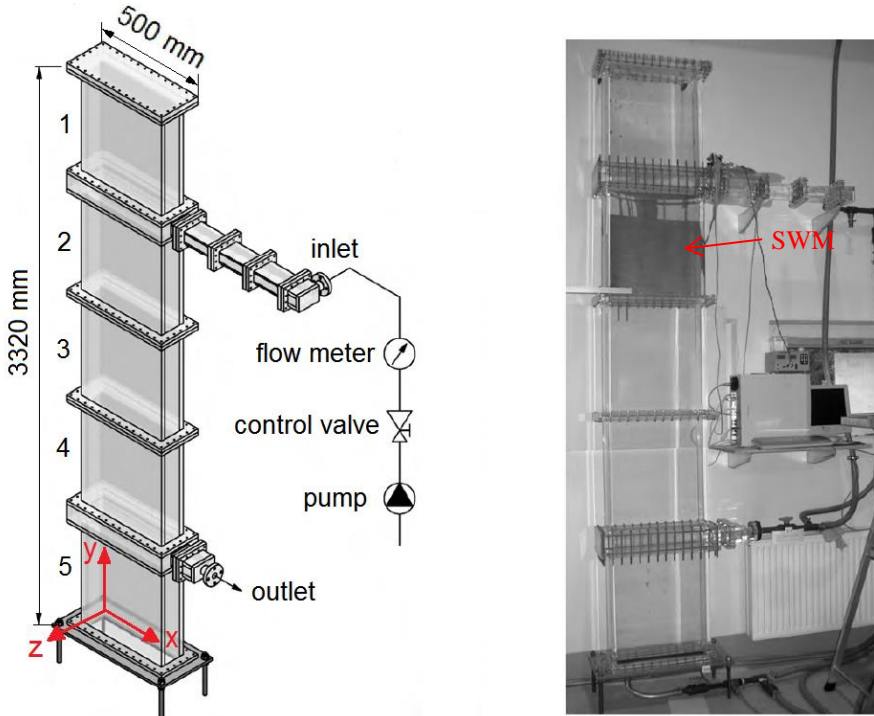


Fig. 1. Schematic view and photograph of the VeMix test facility [18].

In a single experiment under a certain flow condition, water is firstly filled into the test section using the inlet nozzle. Water-sucrose mixture is then very slowly inserted from the bottom up to a certain level, H_{fill} , taking care not to premix both fluids. In this way, a layered structure is obtained with pure water above the water-sucrose

mixture. Finally, the mixing process is initiated by injecting water-sucrose solution through the inlet nozzle with a certain flow rate \dot{V} .

The mixing phenomena was captured with optical methods (high-speed video recording) and surface wire mesh (SWM) measurements by Da Silva et al [18,19]. The video observation method is based on filming the experimental flow phenomena with a high-speed camera, whereby the heavy fluid, i.e. the water-sucrose solution, was dyed with the fluorescent dye yellow uranin. The most interesting location in the VeMix vessel was found to be segment 2, which is just below the inlet nozzle. Therefore, a surface wire mesh sensor based on electrical conductivity measurements was placed here in order to measure the transient behavior of the heavy fluid jet in this area, as shown in Figure 1. The sensor board is designed to fit to the VeMix channel and has a size of $620 \times 500 \text{ mm}^2$. A 64×64 grid corresponding to the measuring points of the surface wire mesh sensor was imported into CFDPost to generate a field to which the experimental and numerical data could be mapped. The frames extracted from the high-speed video as well as the images of the instantaneous density distribution obtained from the surface wire mesh measurements are used to validate the numerical results.

3. Numerical simulation

3.1. Theoretical model

Buoyancy is driven by variations in density which can arise, as in this case, from mass fraction variations caused by local mixing in multicomponent flows. In applying a buoyancy dependent calculation, a body force term, $S_{b,i}$, is added to the momentum equations [1].

$$S_{b,i} = (\rho - \rho_{\text{ref}})g_i \quad (1)$$

Here, $g_i = [0, -9.81, 0] \text{ m/s}^2$ denotes the acceleration due to gravity, which is considered to act vertically downward. The reference density $\rho_{\text{ref}} = \frac{1}{N} \sum_{i=1}^N \rho_i$ is the average density of all N components in the fluid. The fluid density ρ is calculated from the mass fraction w_i and the thermodynamic density ρ_i of each component [1,3]:

$$\frac{1}{\rho} = \sum_{i=1}^N \frac{w_i}{\rho_i} \quad (2)$$

The SST model is widely used for modelling the eddy viscosity in RANS and is important also in corresponding hybrid RANS-LES. The modification of the turbulent transport equations in the SST model to include buoyancy effects is therefore of special importance in this study. The influence of buoyancy on the turbulent transport could be accounted for via an additional source term P_{kb} in the turbulence transport equations for the turbulent kinetic energy k and via a correction term $P_{\omega b}$ for the turbulent eddy frequency ω :

$$\frac{D\bar{\rho}k}{Dt} = \frac{\partial}{\partial x_j} \left[\left(\mu + \frac{\mu_t}{\sigma_{k3}} \right) \frac{\partial k}{\partial x_j} \right] - \beta^* \bar{\rho} k \omega + P_k + P_{kb} \quad (3)$$

$$\frac{D\bar{\rho}\omega}{Dt} = \frac{\partial}{\partial x_j} \left[\left(\mu + \frac{\mu_t}{\sigma_{\omega 3}} \right) \frac{\partial \omega}{\partial x_j} \right] + (1 - F_1) 2\bar{\rho} \frac{1}{\sigma_{\omega 2} \omega} \frac{\partial k}{\partial x_j} \frac{\partial \omega}{\partial x_j} \quad (4)$$

$$+ \alpha_3 \frac{\omega}{k} P_k - \beta_3 \bar{\rho} \omega^2 + P_{\omega b}$$

The right-hand side terms in Equation 3 are the diffusion, the dissipation, the shear production and the buoyancy production term, respectively. σ_{k3} , β^* , $\sigma_{\omega 2}$, $\sigma_{\omega 3}$, α_3 and β_3 are model coefficients. μ denotes the molecular viscosity, μ_t is the turbulent eddy viscosity, F_1 is a blending function limiting ω to the boundary layer, $P_k = -\bar{\rho} \bar{u}'_i \bar{u}'_j (\partial \bar{u}_i / \partial x_j)$ is the production term due to viscous forces [12]. The buoyancy correction term $P_{\omega b}$ is derived from P_{kb} and takes the form

$$P_{\omega b} = \frac{\omega}{k} (\alpha_3 + 1) \max(P_{kb}, 0) - \frac{\omega}{k} P_{kb} \quad (5)$$

The buoyancy production term P_{kb} is related to the gravitational acceleration g_i and the Reynolds-averaged turbulent density fluxes $\bar{\rho}' \bar{u}'_i$:

$$P_{kb} = \sum_{i=1}^3 g_i \bar{\rho}' \bar{u}'_i \quad (6)$$

The Reynolds-averaged turbulent density fluxes could be modelled with second-moment closures in an analogous manner to the turbulence model of thermal

buoyancy-driven flow proposed in Carteciano et al. [2] and in Hanjalić [6].

$$\frac{D\overline{\rho' u'_i}}{Dt} = \frac{\partial}{\partial x_k} \left[\underbrace{\frac{\Gamma}{\bar{\rho}} \frac{\partial \rho'}{\partial x_k} u'_i + \frac{\mu}{\bar{\rho}} \rho' \frac{\partial u'_i}{\partial x_k} - \overline{\rho' u'_i u'_k}}_{D_{\rho'i}^{\mu}} \right] - \underbrace{\frac{\rho' \partial p'}{\bar{\rho} \partial x_i}}_{\Pi_i} - \underbrace{\frac{\Gamma + \mu}{\bar{\rho}} \frac{\partial \rho'}{\partial x_k} \frac{\partial u'_i}{\partial x_k}}_{\varepsilon_{\rho'i}} \\ - \underbrace{\overline{u'_i u'_k} \frac{\partial \bar{\rho}}{\partial x_k}}_{P_{\rho'i}^{\rho}} - \underbrace{\overline{\rho' u'_k} \frac{\partial \bar{u}_i}{\partial x_k}}_{P_{\rho'i}^u} + \underbrace{\frac{g_i}{\bar{\rho}} \overline{\rho'^2}}_{G_{\rho'i}}$$
(7)

Here $D_{\rho'i}$ stands for the total diffusion of $\overline{\rho' u'_i}$ including the molecular diffusion $D_{\rho'i}^{\mu}$ and the turbulent diffusion $D_{\rho'i}^t$, Π_i is the pressure scrambling effect, and $\varepsilon_{\rho'i}$ is the molecular destruction. In addition to the production due to mean density and velocity gradients, $P_{\rho'i}^{\rho}$ and $P_{\rho'i}^u$, respectively, the equation contains a buoyancy production term $G_{\rho'i}$, where the transport equation for the mean density variance $\overline{\rho'^2}$ needs to be considered.

$$\frac{D\overline{\rho'^2}}{Dt} = \frac{\partial}{\partial x_k} \left[\underbrace{\frac{\Gamma}{\bar{\rho}} \frac{\partial \rho'^2}{\partial x_k} - \overline{\rho'^2 u'_k}}_{D_{\rho'^2}^{\mu}} \right] - 2 \underbrace{\frac{\Gamma}{\bar{\rho}} \frac{\partial \rho'}{\partial x_k} \frac{\partial \rho'}{\partial x_k}}_{\varepsilon_{\rho'^2}} - 2 \underbrace{\overline{\rho' u'_k} \frac{\partial \bar{\rho}}{\partial x_k}}_{P_{\rho'^2}}$$
(8)

$$D_{\rho'^2}$$

Here $D_{\rho'^2}$ is the total diffusion of the density variance including the molecular diffusion $D_{\rho'^2}^{\mu}$ and the turbulent diffusion $D_{\rho'^2}^t$. $\varepsilon_{\rho'^2}$ is the molecular destruction term and $P_{\rho'^2}$ is the production term due to mean density gradients.

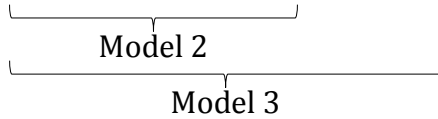
The turbulent shear stresses $\overline{u'_i u'_k}$, which appear in the transport equations for the turbulent density fluxes, are modelled by the isotropic eddy-viscosity hypothesis [1]:

$$\overline{u'_i u'_k} = \frac{2}{3} k \delta_{ik} - \nu_t \left(\frac{\partial \bar{u}_i}{\partial x_k} + \frac{\partial \bar{u}_k}{\partial x_i} \right) \quad (9)$$

A DNS-based term-by-term scrutiny of models of various terms in the transport equations for the turbulent scalar fluxes was carried out in Hanjalić [6]. It was concluded that even if most of the terms can be modelled to reproduce DNS results in

some generic situations, their validity for complex flows still remains questionable, and a full implementation of such differential second-moment closure requires a substantial computational effort. For practical application simpler models should be developed, which do not require solutions of differential transport equations for each stress and flux component, but can still capture important physical processes. By assuming that the production and dissipation of both k and $\bar{\rho}'^2$ are locally in balance, the transport terms in Equation 7 could be neglected and the differential equations for the second moments can be truncated to yield algebraic expressions for turbulent density fluxes [17]. Neglecting the molecular destruction term $\varepsilon_{\rho'i}$ and certain production terms leads to a further simplification. In this work, three different algebraic flux models, which have different levels of physical approximation, were implemented into Ansys CFX:

$$\overline{\rho' u'_i} = -\tau_t \left(\underbrace{\overline{u'_i u'_k} \frac{\partial \bar{\rho}}{\partial x_k}}_{\text{Model 1}} + \xi \overline{\rho' u'_k} \frac{\partial \bar{u}_i}{\partial x_k} - \frac{\eta}{\bar{\rho}} g_i \overline{\rho'^2} \right) \quad (10)$$



Here the turbulent time scale is defined as $\tau_t = C^{\rho'} \frac{k}{\varepsilon}$ with $C^{\rho'} = 0.1$, and $\xi = \eta = 0.45$ are model constants [6]. In Model 1 only the production term due to the mean density gradient is included, which is also known as the generalized gradient diffusion hypothesis. It should be noted that replacing the Reynolds stress $\overline{u'_i u'_k}$ by its trace $\overline{u'_i u'_i} = 2k$ leads to the isotropic eddy-diffusivity hypothesis:

$$\overline{\rho' u'_i} = -\frac{\mu_t}{\bar{\rho} S c_t} \frac{\partial \bar{\rho}}{\partial x_i} \quad (11)$$

which is applied in the standard turbulent buoyancy model in Ansys CFX. Here $S c_t$ is the turbulent Schmidt number and is set to 1 in the standard buoyancy model [1].

In Large Eddy Simulation, buoyancy effects are taken into account via the source terms in the governing equations for the resolved flow. However, their contribution to turbulent production through unresolved scales requires proper subgrid-scale models. Eidson [4] proposed to include the SGS buoyant production in the local equilibrium argument for flows driven by thermal buoyancy. Substituting the temperature gradients with the density gradients leads to a SGS model where the buoyant

production is directly evaluated with the resolved density distribution:

$$\mu_{sgs} = \frac{\bar{\rho}(C_s \Delta)^2}{\tau_{sgs}} \quad (12)$$

$$\tau_{sgs} = \left(|\bar{S}|^2 - \frac{1}{\bar{\rho} S c_{sgs}} \frac{\partial \bar{\rho}}{\partial x_i} g_k \delta_{kj} \right)^{-1/2} \quad (13)$$

Here τ_{sgs} is the SGS time scaling, $|\bar{S}|$ is the magnitude of the mean strain rate tensor. $S c_{sgs} = 0.9$ denotes the SGS Schmidt number. C_s is the Smagorinsky constant and was taken as 0.21 in the present study [4]. To avoid rendering non-real solutions, it is necessary to constrain the instantaneous SGS viscosity μ_{sgs} to be equal to zero as $|\bar{S}|^2 - \frac{1}{\bar{\rho} S c_{sgs}} \frac{\partial \bar{\rho}}{\partial x_i} g_k \delta_{kj} < 0$. Winckelmans et al. [23] evaluated several base models with different choices for the SGS time scaling τ_{sgs} and found that the SGS time scaling does not significantly affect the correlations between the modified and exact SGS quantities. This suggests that τ_{sgs} does not necessarily need to be derived from the production-dissipation equilibrium argument. In order to relax this constraint of the SGS viscosity, Peng & Davidson [16] proposed using $|\bar{S}|$ to weight the Eidson time scaling, which leads to a form of the SGS eddy viscosity as follows:

$$\mu_{sgs} = \bar{\rho}(C_s \Delta)^2 \left(|\bar{S}| - \frac{1}{\bar{\rho} S c_{sgs} |\bar{S}|} \frac{\partial \bar{\rho}}{\partial x_i} g_k \delta_{kj} \right) \quad (14)$$

Here μ_{sgs} allows negative values as a way of representing energy transfer from the small scales to the large ones. It should be noticed that the total viscosity, $(\mu_{sgs} + \mu)$, should be positive in order to retain numerical stability [16].

In summary, following buoyancy-modified models were applied in the current study:

Tab. 1. Turbulence models and their abbreviation used in the current study.

Buoyancy models	SST	SBES	SAS
Without buoyancy model	SSTnone	SBESnone	SASnone
CFX standard buoyancy model	SSTPD	SBESPD	SASPD
Algebraic flux model 1/2/3	SSTMo1/2/3	SBESMo1/2/3	SASMo1/2/3
Smagorinsky SGS model	LES		
Eidson SGS model	LES Eidson		
Peng SGS model	LES Peng		

3.2. Numerical setup

A mesh independence study was conducted with the SST model, the results of which are also important for the SST-based hybrid models (SAS, SBES). As the density distribution near the inlet nozzle is dominated by the mixing process rather than by the wall shear stress, resolving the wall boundary layers, which requires a high computational effort due to wall refinement, should not improve the results of interest considerably. A special wall treatment was therefore applied for all the turbulence models mentioned in this work, which automatically switches between the wall function approach and the integration to wall approach depending upon the dimensionless wall distance $y^+ = y\sqrt{\tau_w\rho}/\mu$. Here y denotes the distance from the first grid point to the nearest wall and τ_w is the wall shear stress [1]. As the requirement on the grid size near the wall is relaxed by the wall function, three uniform meshes have been generated and the mesh parameters are shown in Table 2. The density profiles along a vertical monitoring line $x = 0.35$ m, $z = 0.05$ m and the oscillation frequencies of the inlet flow jet under the flow conditions $\Delta\rho = 2\%$, $\dot{V} = 0.45$ l/s, $H_{\text{fill}} = 2$ m are shown in Figures 2(a) and 2(b), respectively. Due to the heavy fluid jet, the density reaches its peak at the height of the inlet nozzle at about $y = 2.6$ m. Compared to the results obtained by the middle mesh and the fine mesh, the peak position is slightly shifted and the peak value is lower on the coarse mesh. The oscillation frequency tends to increase with increasing number of mesh elements. This is assumed to be related to the large numerical dissipation on coarse mesh, which results in a suppression of the vortex. As there are only slight differences between the results obtained by the middle mesh and by the fine mesh, the middle mesh of approximately 3.3×10^5 elements is a good compromise between computational effort and accuracy of results.

Tab. 2. Mesh parameters of mesh independence study.

Mesh	Number of elements	Discretization settings (mm)	Max. y^+
Coarse	66280	$\Delta x = 10, \Delta y = 10, \Delta z = 40$	200
Middle	332900	$\Delta x = 5, \Delta y = 5, \Delta z = 20$	100
Fine	2663200	$\Delta x = 2.5, \Delta y = 2.5, \Delta z = 10$	50

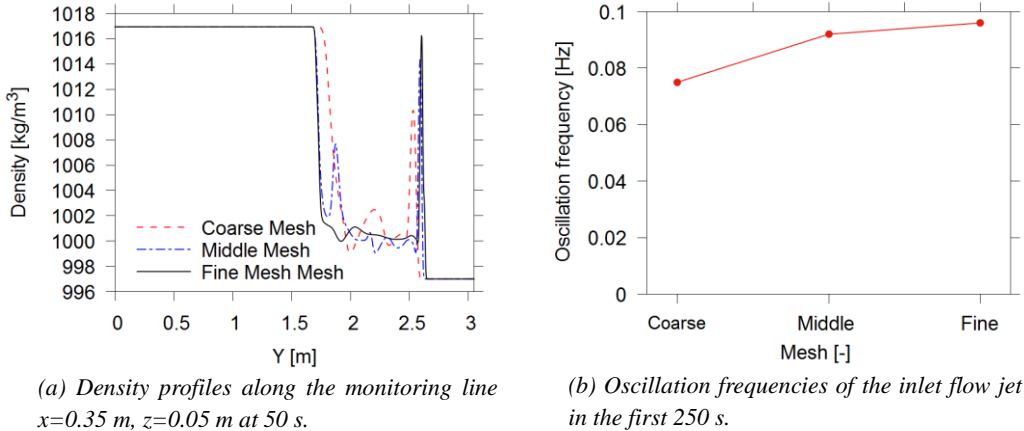


Fig. 2. Results of mesh independence study under the flow conditions $\Delta\rho = 2\%$, $\dot{V} = 0.45 \text{ l/s}$, $H_{\text{fill}} = 2 \text{ m}$.

For the LES model, following the idea that a sizeable amount of the turbulent kinetic energy should be resolved, the quality of the middle mesh is checked by estimating the ratio between the unresolved turbulent kinetic energy k_{sgs} and the total turbulent kinetic energy under the flow conditions $\Delta\rho = 2\%$, $\dot{V} = 0.45 \text{ l/s}$, $H_{\text{fill}} = 2 \text{ m}$ [5].

$$K^* = \frac{k_{\text{sgs}}}{k_{\text{sgs}} + 1/2(\bar{u}_i' \bar{u}_i' + \bar{u}_j' \bar{u}_j' + \bar{u}_k' \bar{u}_k')} \quad (15)$$

Here k_{sgs} is evaluated based on the SGS viscosity [10]:

$$k_{\text{sgs}} = \sqrt{\frac{\mu_{\text{sgs}}^2 |\bar{S}|^2}{\bar{\rho}^2 C_\mu}} \quad (16)$$

with $C_\mu = 0.09$ being a constant. The so calculated ratio between the unresolved and the total turbulent kinetic energy is averaged over the first 250 s and ranges between 0 and 0.2 in the main mixing zone. Considering the threshold of $K^* = 0.2$ for well-resolved LES simulations given in [5], the middle mesh should be fine enough for the LES simulations. Therefore, the middle mesh was used for all the turbulence models in this work.

For the transient simulation, the time integration was carried out using the second order backward Euler scheme. In order to avoid incorrect solution, the time step size Δt should be adjusted so that the Courant-Friedrichs-Lowy number $CFL = u\Delta t/\Delta x$ is lower than 1 for the Scale-Resolving Simulations [13]. As a compromise between accuracy and robustness of the calculation, the high resolution scheme was selected for the advection terms of the momentum transport equations in SST. For SRS, the

dissipation is provided by the LES eddy viscosity model and thereby the second order central difference scheme with low dissipation was selected [13]. The turbulence equations, in contrast, are not sensitive to the spatial discretization schemes used for the advection terms. The first order upwind scheme is therefore sufficient for the turbulence equations. According to a sensitivity study of the convergence criteria, the target RMS residual is set to 10^{-4} for all the simulations to ensure sufficient accuracy.

The initial condition for the mass fraction of the heavy fluid in the simulations corresponds to the initial fill height of the heavy fluid H_{fill} , which is varied according to the case studies. Due to the no-slip condition, the fluid velocity at all the walls should be zero. The velocity profile at the inlet nozzle is calculated from the flow rate and the cross-sectional area of the inlet nozzle. It was observed in the experiments that in the first several seconds, instead of the heavy fluid, a remainder of light fluid in the pipeline system was injected in the vessel. This period of time is dependent on the volume of the light fluid remainder and the flow rate. It was reported in Vaibar [22] and observed in the present study that neglecting of this phenomena can lead to incorrect results in the simulations. Therefore, the light fluid remainder in the pipeline should always be considered.

4. Results

4.1 Flow characterization

In the experimental study, two main flow regimes were observed: The falling down regime and the horizontal jet regime. As shown in Figure 3(a), with a high flow rate of $\dot{V} = 0.7 \text{ l/s}$, the gravity force is significantly weaker than the inertia force driven by input flow rate, which generates a horizontal jet of the heavy fluid. With a lower flow rate of $\dot{V} = 0.4 \text{ l/s}$, the gravity force is stronger than the inertia force and the jet drops near the vertical side wall, as shown in Figure 3(b). These different flow regimes in the VeMix facility are significantly influenced by the ratio between the buoyancy and the inertia forces, which can be characterized by the Richardson number Ri [3, 8, 19].

$$Ri = \frac{gL\Delta\rho}{\rho_l v^2} \quad (17)$$

Here $\Delta\rho$ is the density difference between the two fluids, $\rho_l = 997 \text{ kg/m}^3$ is the density of the light fluid, v is the characteristic velocity and corresponds to the ratio between the flow rate and the cross-sectional area of the VeMix main vessel. In the present study, the distance between the inlet and the outlet nozzle is chosen to be the characteristic length L . This corresponds to the height of the PWR downcomer, which is usually defined as the characteristic length in studies of the density-driven coolant mixing in the PWR [3, 8].

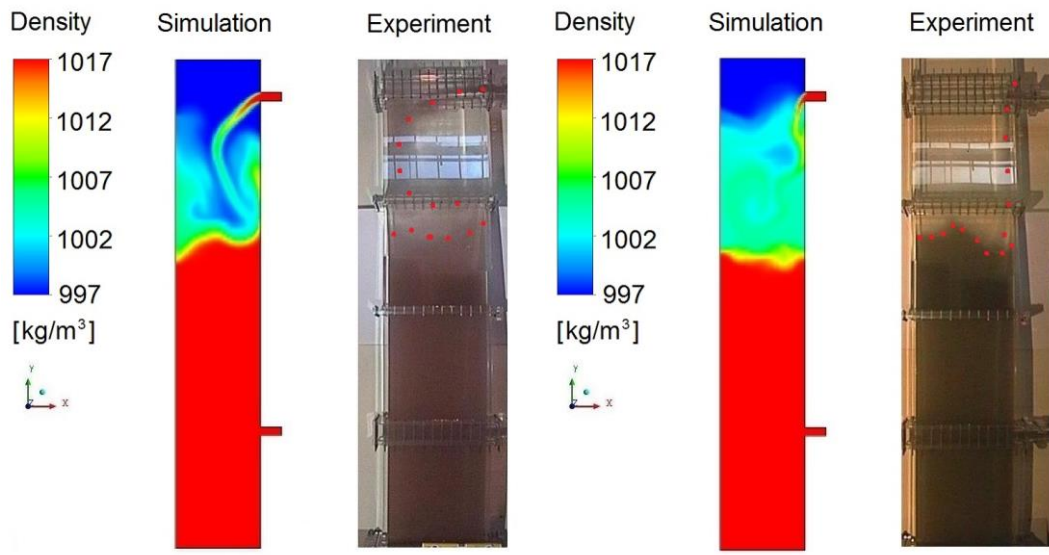


Fig. 3. Flow regime under the flow conditions $\Delta\rho = 2\%$, $H_{\text{fill}} = 1.8 \text{ m}$. Dotted lines illustrate the heavy fluid jet and the interface between the heavy and the light fluids in the photos obtained by high-speed camera.

In order to study the influence of the Richardson number on the flow regimes, simulations of different flow conditions with different Richardson numbers have been performed, using the standard buoyancy-modified SST model. As the characteristic length L and the density of the light fluid ρ_l are kept constant, the Richardson number is only dependent on the initial density difference $\Delta\rho$ (buoyancy forces) and the flow rate \dot{V} (inertia forces). The flow regimes in the first 100 s obtained under different flow conditions are summarized in Figure 4. It could be concluded that in the region of $Ri > 30$, the injected heavy fluid usually drops near the vertical side wall, while a horizontal jet regime was usually predicted when $Ri < 20$. Both flow regimes appear in the transition area of $20 < Ri < 30$, as the

gravity and inertia forces are of comparable size.

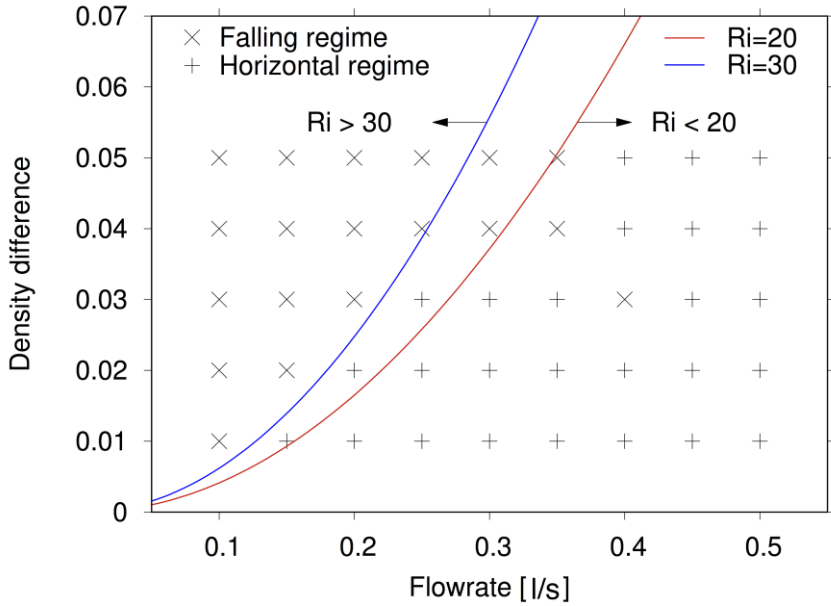


Fig. 4. Influence of Ri on flow regime.

4.2 Qualitative Results

As mentioned above, a surface wire mesh sensor was placed below the inlet nozzle in order to study the mixing process in this area. Direct comparisons of the density distribution in the area of the surface wire mesh sensor were conducted at times 25 s and 50 s. The flow conditions ($\Delta\rho = 2\%$, $\dot{V} = 0.5 \text{ l/s}$, $H_{\text{fill}} = 2.07 \text{ m}$) result in a low Richardson number of 3.87, which indicates that the gravity forces are significantly weaker than the inertia forces and a horizontal flow regime is to be expected. At time 25 s, the heavy and the light fluids are not yet well mixed and a strong jet can be observed in both experiment and simulations. The results obtained by different models are very similar to each other. With regard to the shape and the injection angle of the heavy fluid, SRS models achieve better agreement with experiment than the SST model. Besides, the jet calculated by the SST model seems to be very stable and the detailed turbulent structures observed in experiment and in SRS simulations are averaged out. The horizontal jet predicted by the buoyancy-modified SGS models is wider than by the standard Smagorinsky model where the buoyancy-generated turbulence is not considered. But in general, influences of different buoyancy terms on the calculated density distribution are not significant.

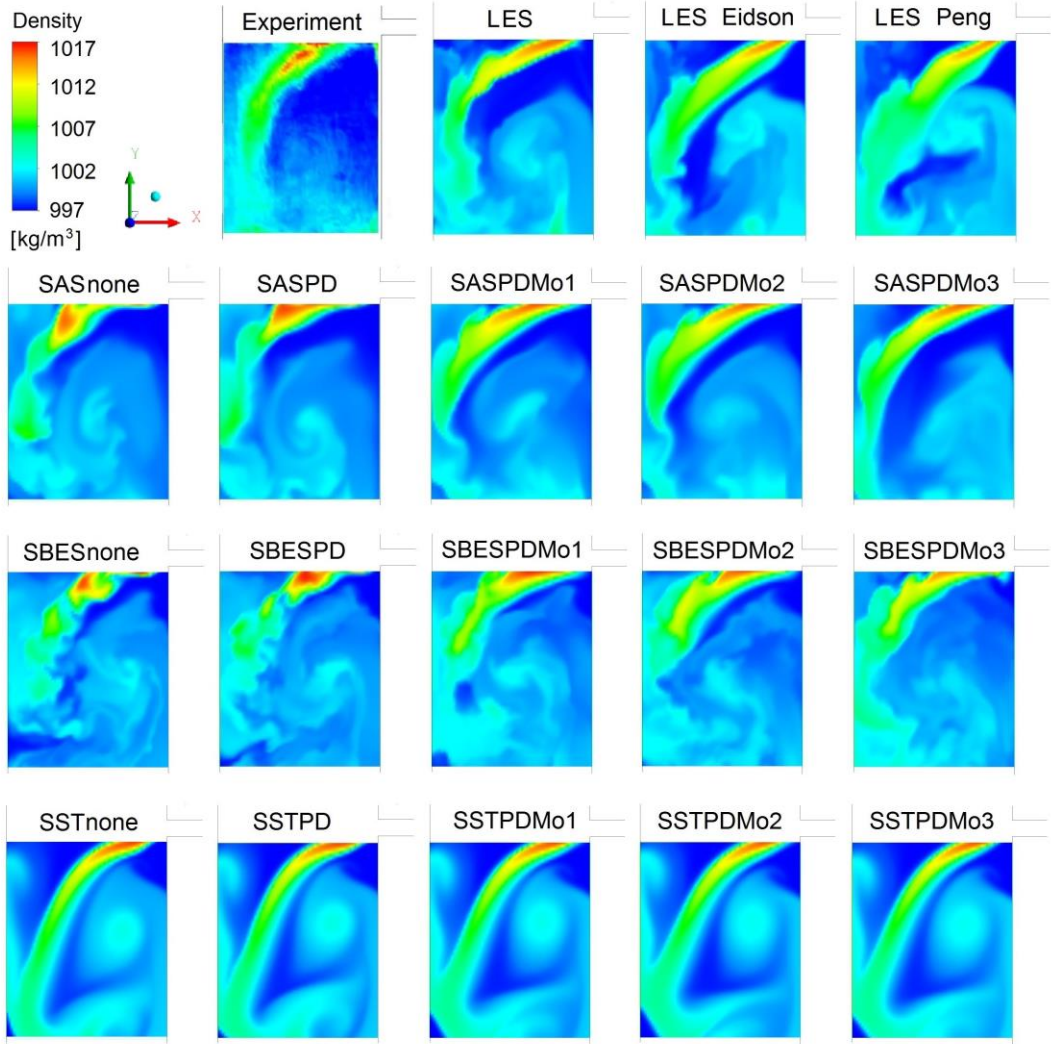


Fig. 5. Density distribution in the area of the surface wire mesh sensor at time 25 s.

At time 50 s, as shown in Figure 6, the differences between the different models become more obvious. The SST model seems to have calculated a jet which has moved above the upper boundary of the surface sensor. In comparison, the simulation results with SRS models are qualitatively more similar to the experimental data and the best performance is achieved by SBES and LES. Compared to the CFX standard model, where the isotropic eddy-diffusivity hypothesis is applied, a slight improvement regarding the shape of the heavy fluid jet has been achieved by the anisotropic new buoyancy models in SAS and SST. In LES, the differences between the models are very small and the buoyancy-modified SGS models have not shown superiority compared to the standard Smagorinsky model. In general, the discrepancies between experimental results and numerical results obtained by the

RANS-based SST models are still large, while SRS models show a good agreement with the experiment.

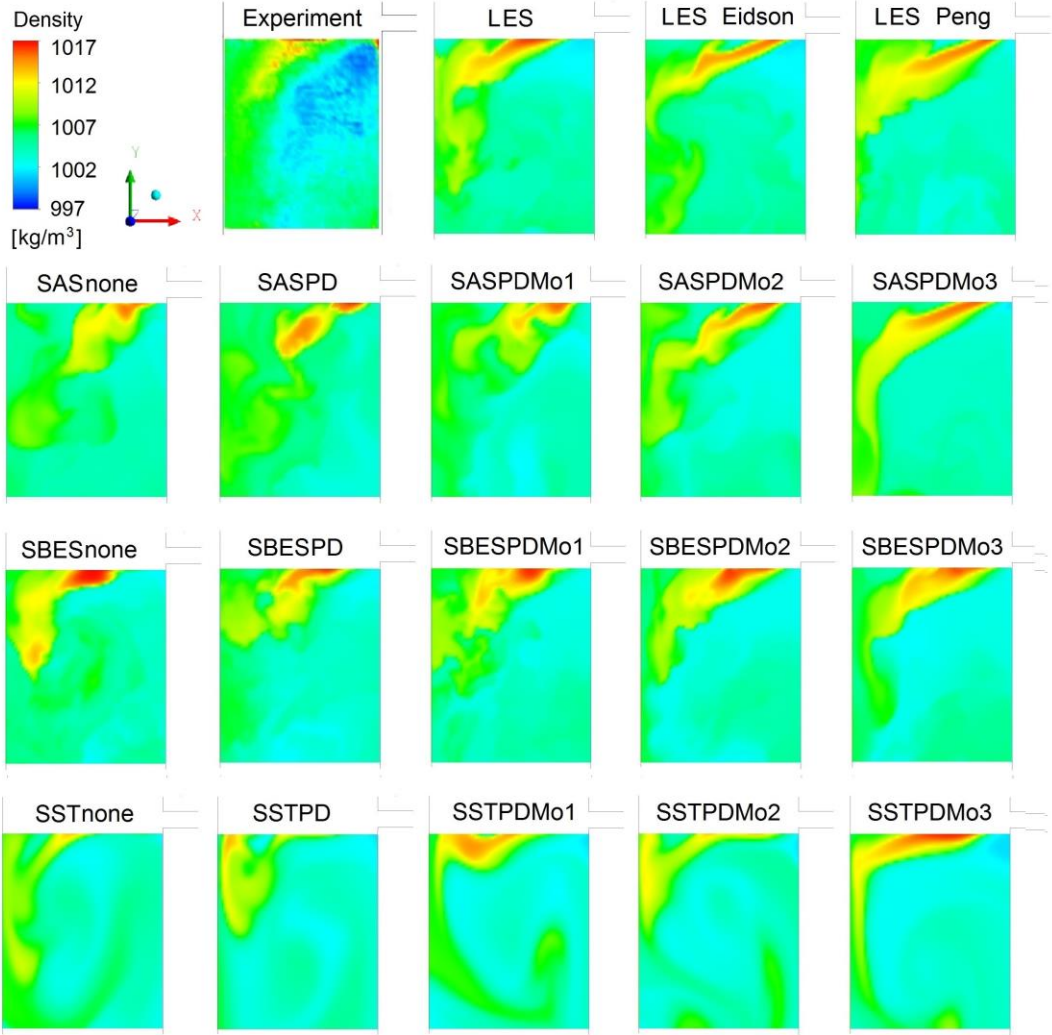


Fig. 6. Density distribution in the area of the surface wire mesh sensor at time 50 s.

4.3 Quantitative Results

In the horizontal jet regime, oscillatory, wave-like instabilities related to strong density oscillations are formed at the interface between light and heavier fluids. To quantitatively describe the behavior of these density oscillations, the 3 components of video signal (RGB) from the digital camera and from the simulations are analyzed. A point above the inlet nozzle $x = 0.1$ m, $y = 2.7$ m, $z = 0.05$ m was chosen as the monitoring point, where strong oscillations of the RGB colors of the mixed fluid are observed in experiment and in simulations. The significant frequency of the Fourier

Power Spectral Density (PSD) of the RGB signal at the observing point characterizes the strength of the density fluctuations and corresponds to the energy in the density oscillations. Figure 7(a) shows the significant frequency in the first 250 s calculated by different turbulence models with or without the buoyancy source terms under the flow conditions $\Delta\rho = 2\%$, $\dot{V} = 0.45 \text{ l/s}$, $H_{\text{fill}} = 2 \text{ m}$, $Ri = 4.78$. In general, all the models have captured the measured significant oscillation frequency of about 0.09. Only in the SAS simulation without buoyancy model, the fluctuations are evenly distributed over all the frequencies and a significant frequency could not be found. It should also be noticed that the calculated significant frequencies with the activation of the buoyancy model (“PD”) are usually higher than that without the buoyancy model (“None”), meaning that in the models where the buoyancy-generated turbulence is accounted for, the oscillation energy is contained by higher frequencies than in the models where the buoyancy effects on the turbulence are neglected. These discrepancies are assumed to be related to the different eddy viscosity levels. It was noticed that the eddy viscosity in the “None” models is generally slightly higher than the corresponding “PD” models. An example is shown in Figure 7(b), where the distributions of the time-averaged eddy viscosity in the vertical middle plane of the VeMix device calculated by the SST model with or without activation of the buoyancy model are illustrated. It is obvious that including the buoyancy terms (“PD” models) reduces the eddy viscosity and the associated viscous damping effects, causing the oscillation frequencies generally higher than those obtained by the “None” models. Considering the fact that density differences and the associated buoyancy effects do exist in the reality, and that the “None” models have not shown any superiority compared to the “PD” models, it is reasonable to always activate the buoyancy terms in similar cases.

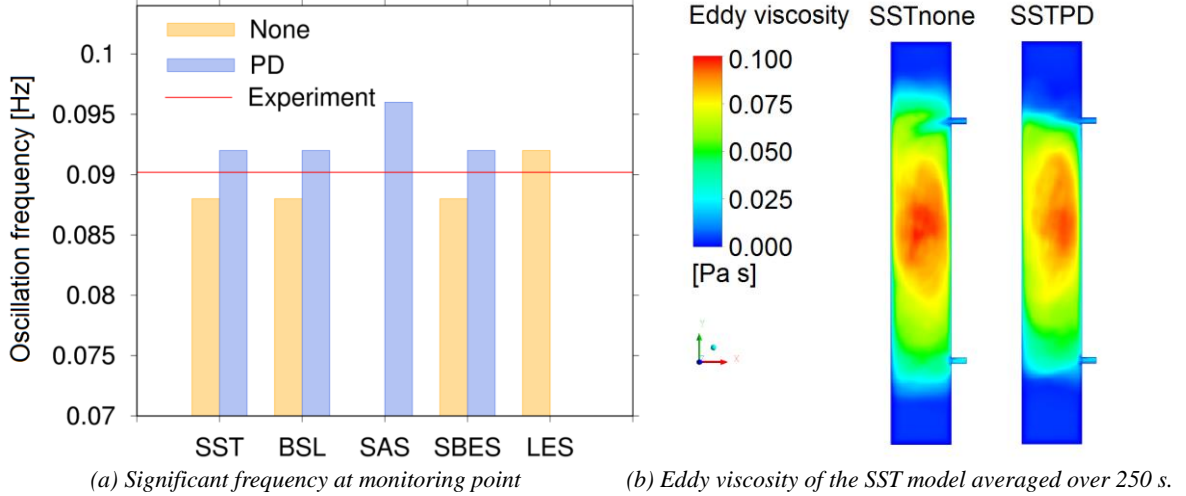


Fig. 7. Oscillation frequencies of the inlet horizontal jet and the time-averaged eddy viscosity in the vertical middle plane.

To study the influence of flow conditions on the transient mixing process, experiments with flow rates 0.35 l/s, 0.4 l/s, 0.45 l/s and 0.5 l/s have been carried out [21], where the other parameters are fixed at $\Delta\rho = 2\%$, $H_{\text{fill}} = 2$ m. The Richardson number under such flow conditions ranges from 3.87 to 7.90, indicating that a horizontal jet should be expected and the oscillation frequencies of it can be used to evaluate the different turbulence models. The oscillation frequencies at different flow rates are extracted with the Fourier transformation and shown in Figure 8. According to the experimental data, there is a trend of the frequency to rise with increasing flow rate, which is also found in the simulations. In the SST simulations, at a comparatively high flow rate of 0.5 l/s, the standard SST model (SSTPD) and the new buoyancy model, Mo3, predicted a frequency which is 6% lower than the measured frequency. This difference is reduced to 2% by using the buoyancy model Mo1 or Mo2. At lower flow rates, Mo2 shows superiority comparing to Mo1, as the latter has overpredicted the frequency. In the SAS simulations, the standard buoyancy model tends to overpredict the frequency. The performance is improved in modified buoyancy models especially in Mo2. At a flow rate of 0.5 l/s, Mo2 and Mo3 have slightly underpredicted the oscillation frequency in SBES. The largest discrepancy between numerical and experimental results is that the standard SBES model has predicted a frequency which is 9% higher than the experiment at a flow rate of 0.4 l/s. An improvement of the results is achieved especially by Mo1 in SBES. In the LES simulations, the frequencies predicted by the SGS model without modelling the buoyancy-induced turbulence are exactly the same as the ones predicted by the

buoyancy-modified Eidson model, and both are in very good agreement with the experiment. The Peng model tends to slightly overpredict the frequencies. But from an experimental point of view, these differences are not significant, showing the superiority of LES of capturing the transient flow characteristics.

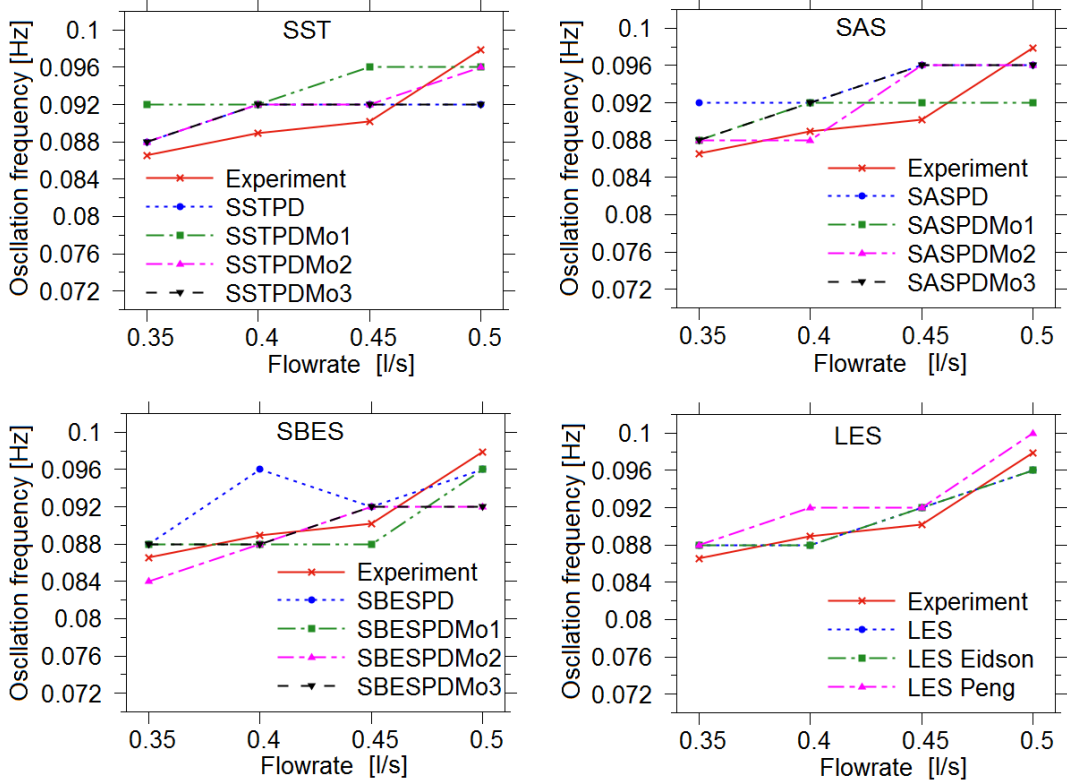


Fig. 8. Oscillation frequencies obtained by different buoyancy-modified turbulence models.

4.4 Analysis of the influence of the buoyancy-generated turbulence

During the simulations with the standard buoyancy models under the flow conditions $\Delta\rho = 2\%$, $\dot{V} = 0.45 \text{ l/s}$, $H_{\text{fill}} = 2 \text{ m}$, $Ri = 4.78$, different buoyancy production terms defined by the three algebraic flux models described in Equations 6 and 10 have been calculated as well, so that the influence of the buoyancy production terms in RANS and hybrid models could be evaluated intuitively. The calculated buoyancy source terms are averaged over the period of 250 s physical time and are presented along a vertical monitoring line $x = 0.35 \text{ m}$, $z = 0.05 \text{ m}$ in Figure 9. As the monitoring line is near to the inlet nozzle, the buoyancy source terms reach its peak at the height of the inlet nozzle at about $y = 2.6 \text{ m}$ due to the influence of the heavy

fluid injection and the associated high velocity and density gradients in this area. Here the curves are rescaled in order to better illustrate the differences between the different buoyancy models.

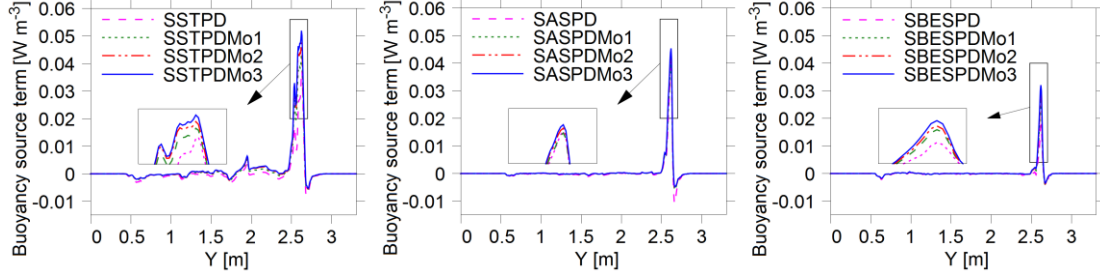


Fig.9. Comparison of time-averaged buoyancy source terms along the vertical monitoring line.

As shown in Figure 9, the influence of different buoyancy models in RANS is more obvious than in hybrid models, because the entire turbulence spectrum in RANS has to be modelled, and the buoyancy effects are accounted for by including the buoyancy source terms in the turbulence equations. The introduction of the isotropic eddy-diffusivity hypothesis in the standard buoyancy model results in a weaker buoyancy source term on the entire monitoring line. The differences between the new developed algebraic models are negligible except in the near of the inlet nozzle. But even in this area the differences are relatively small, suggesting that the second and third terms in Equation 10 only play a minor role, and the buoyancy-induced turbulence is mainly provided by the mean density gradient.

The influence of buoyancy-induced turbulence in RANS and in hybrid models is further evaluated by analyzing the magnitude of the time-averaged diffusion, dissipation, and production terms in the transport equation for the turbulent kinetic energy (Equation 3) [11]. The results are illustrated in Figure 10. As the differences between the magnitudes of buoyancy source terms in different models are not significant, only the buoyancy production terms provided by Model 1 are presented.

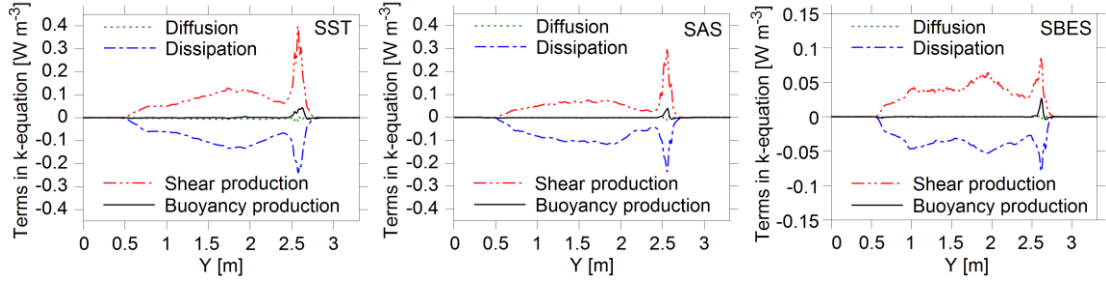


Fig. 10. Comparison of time-averaged terms in the transport equation for the turbulent kinetic energy along the vertical monitoring line.

It is obvious that the turbulent kinetic energy is dominated by the shear production term P_k and the dissipation term $\beta^* \bar{\rho} k \omega$ in each turbulence model. The peak is at about $y = 2.6$ m, where the heavy fluid is injected into the vessel, which produces high shear stresses and density gradients in this area. The diffusion term is negligible and only in the near of the inlet nozzle, the buoyancy effects can be identified. Here the buoyancy production P_{kb} ranges from 10% to 30% of the shear production term P_k in different models and should not be neglected. If P_{kb} is not included in the k -equation, the eddy viscosity tends to be slightly overpredicted and the oscillation frequency tends to be underpredicted, as shown in Figure 7. The right hand side terms in the k -equation in SBES are substantially lower than those in other turbulence models, which can be related to the low level of the eddy viscosity in SBES.

In LES, the buoyancy-generated turbulence is accounted for in the SGS models by modifying the SGS eddy viscosities. The time-averaged SGS eddy viscosities along the vertical monitoring line $x = 0.35$ m, $z = 0.05$ in different models are presented in Figure 11. Above the inlet nozzle at $y = 2.8$ m, a negative density gradient exists and the buoyancy-modified SGS viscosity is lower than the standard Smagorinsky eddy viscosity, which can be explained by Equations 13 and 14. The peak of the eddy viscosity at $y = 2.6$ m corresponds to the high velocity gradient and the associated high shear strain rate in this area. The high positive density gradient due to the injection of the heavy fluid leads to a minor increase in the eddy viscosity in buoyancy-modified SGS models at $y = 2.6$ m. But in general, the introduction of the buoyancy terms in SGS models has only a minor influence on the calculated SGS eddy viscosity.

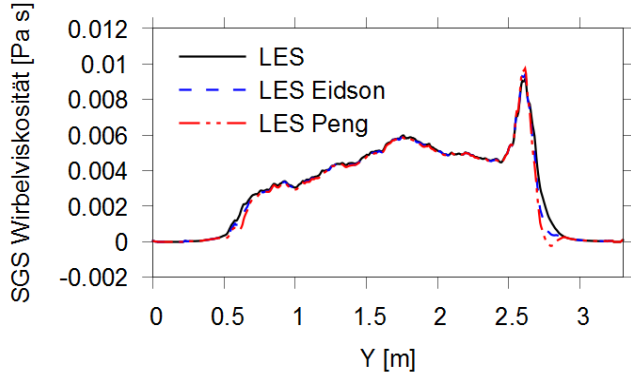


Fig. 11. Time-averaged SGS eddy viscosity calculated for different SGS models on the vertical monitoring line.

The influence of the SGS model on the resolved flow field is evaluated by comparing the magnitude of different terms in the filtered momentum equations in LES:

$$\frac{D\bar{\rho}\bar{u}_i}{Dt} = -\frac{\partial \bar{p}}{\partial x_i} + \frac{\partial}{\partial x_j} (2\mu \bar{S}_{ij}) + \frac{\partial \tau_{ij}^{\text{sgs}}}{\partial x_j} + \bar{F}_i \quad (18)$$

The right-hand side terms are the momentum source due to pressure gradient, the molecular diffusion term, the divergence of the SGS stress tensor and the resolved buoyancy force, respectively. In order to evaluate the influence of the SGS stress on the filtered momentum equations, the magnitude of the right-hand side terms in Equation 18 are calculated during a simulation with the Smagorinsky SGS model under the flow conditions $\Delta\rho = 2\%$, $\dot{V} = 0.45 \text{ l/s}$, $H_{\text{fill}} = 2 \text{ m}$, $Ri = 4.78$. The order of magnitude of the four terms in the filtered momentum equation in x -, y -, and z -directions are listed in Table 3.

Tab. 3. Order of magnitude of terms in filtered momentum equations in LES.

	Pressure gradient	Molecular diffusion	SGS diffusion	Buoyancy
x -direction	-1	-3	-4	0
y -direction	1	-3	-3	1
z -direction	3	-5	-4	0

It is obvious that the momentum source due to pressure gradient and the resolved buoyancy forces are significantly higher than other terms and the momentum equations are thereby dominated by these two terms. Therefore, the SGS model should only have a minor influence on the resolved flow field, which corresponds to the small differences between the different SGS models.

5. Conclusions

A numerical investigation has been performed in order to study mixing phenomena between miscible fluids of different densities and to validate different buoyancy-modified turbulence models. In comparison to the CFX standard buoyancy model, where the isotropic eddy-diffusivity hypothesis is applied to the turbulent density fluxes [1], a slight improvement of the results with respect to the oscillation behavior of the inlet heavy fluid jet were achieved by new buoyancy models which include the anisotropic buoyancy terms. The differences between the SGS models with or without considering the buoyancy effects are not significant.

By calculating different terms in the transport equations for the turbulent kinetic energy in the SST and hybrid models, it was found that the buoyancy source term produced by the isotropic buoyancy model is slightly lower than for the anisotropic models, and the anisotropic buoyancy model is dominated by the mean density gradient term. The magnitude of the buoyancy source term ranges from 10% to 30% of the shear production term under the flow conditions in this work and neglecting the buoyancy source terms generally results in underpredicted oscillation frequencies. Calculations of different terms in the filtered momentum equations in LES show that the resolved flow is dominated by the resolved pressure term and the resolved buoyancy term, which are significantly higher than the SGS diffusion term. This can explain the small differences between results obtained by different SGS models. With respect to the accuracy of the results, the calculation time and the modelling complexity, Stress-blended Eddy Simulation with modified buoyancy model (Mo1) and Large Eddy Simulation with Eidson buoyancy-modified SGS model are recommended for future simulations at similar flow conditions.

Acknowledgements

The authors would like to thank Prof. J. Fröhlich, Dr. G. Mutschke, T. Hanisch, and Dr. T. Ma for their valuable discussion on this work.

References

- [1] *CFX 18.0 Documentation, ANSYS CFX-Theory Guide*. Ansys, Inc., 2017.
- [2] Carteciano, L. N., Weinberg, D., Müller, U., 1997. Development and analysis of a turbulence model for buoyant flows. In: 4th World Conference on Experimental Heat Transfer, Fluid Mechanics and thermodynamics, Brussels, Belgium, June 2-6.
- [3] Cotton, M. A., Galindo Garcia, I. F., Axcell, B. P., 2013. On the role of buoyancy in determining the course of PWR boron dilution transients. *Applied Thermal Engineering*. 58, pp. 430-438.
- [4] Eidson, T. M., 1985. Numerical simulation of the turbulent Rayleigh-Bénard problem using subgrid modelling. *Journal of Fluid Mechanics*. 158, pp. 245-268.
- [5] Fröhlich, J., von Terzi, D., 2008. Hybrid LES/RANS methods for the simulation of turbulent flows. *Progress in Aerospace Sciences*. 44, pp. 349-377.
- [6] Hanjalić, K., 2002. One-point closure models for buoyancy driven turbulent flows. *Annual Review of Fluid Mechanics*. 34, pp. 321-347.
- [7] Höhne, T., Kliem, S., Bieder, U., Weiss, F.-P., 2008. Boron dilution transients during natural circulation flow in PWR – Experiments and CFD simulations. *Nuclear Engineering and Design*. 238, pp. 1987-1995.
- [8] Höhne, T., Kliem, S., Bieder, U., 2018. IAEA CRP benchmark of ROCOM PTS test case for the use of CFD in reactor design using the CFD-Codes ANSYS CFX and TrioCFD. *Nuclear Engineering and Design*. 333, pp. 161-180.
- [9] Kliem, S., Sühnel, T., Rohde, U., Höhne, T., Prasser, H.M., Weiss, F.-P., 2008. Experiments at the mixing test facility ROCOM for benchmarking of CFD codes. *Nuclear Engineering and Design*. 238, pp. 566-576.
- [10] Ma, T., Zeigenhein, T., Lucas, D., Krepper, E., Fröhlich, J., 2015. Euler-Euler large eddy simulations for dispersed turbulent bubbly flows. *International Journal of Heat and Fluid Flow*. 56, pp. 51-59.
- [11] Ma, T., Santarelli, C., Zeigenhein, T., Lucas, D., Fröhlich, J., 2017. Direct numerical simulation-based Reynolds-averaged closure for bubble-induced turbulence. *Physical Review Fluids*. 2, p. 034301.
- [12] Menter, F. R., 1994. Two-equation eddy-viscosity turbulence models for engineering applications. *AIAA Journal*. 32, pp. 1598-1605.

- [13] Menter, F. R., 2015. Best Practice: Scale-Resolving Simulations in ANSYS CFD. ANSYS Inc., Canonsburg, USA.
- [14] Menter, F. R., 2016. Stress-Blended Eddy Simulation (SBES) – a new paradigm in hybrid RANS-LES modeling. In: 6th HRLM Symposium, Strasbourg, France, September 26-28.
- [15] Menter, F. R., Egorov, Y., 2010. Scale-Adaptive Simulation method for unsteady flow predictions. Part 1: Theory and model description. Journal Flow Turbulence and Combustion. 85, pp. 113-138.
- [16] Peng, S. H., Davidson, L., 1998. Comparison of subgrid-scale models in LES for turbulent convection flow with heat transfer. In: 2nd EF Conference in Turbulent Heat Transfer, pp. 5.24-5.35, Manchester, UK.
- [17] Rodi, W., 1976. A new algebraic relation for calculating the Reynolds stresses. Zeitschrift für angewandte Mathematik und Mechanik. 56, pp. T219-T221.
- [18] Da Silva, M. J., Sühnel, T., Schleicher, E., Vaibar, R., Lucas, D., 2007. Planar array sensor for high-speed component distribution imaging in fluid flow applications. Sensors. 7, pp. 2430-2445.
- [19] Da Silva, M. J., Thiele, S., Höhne, T., Vaibar, R., Hampel, U., 2010. Experimental studies and CFD calculations for buoyancy driven mixing phenomena. Nuclear Engineering and Design. 240, pp. 2185-2193.
- [20] Smagorinsky, J., 1963. General circulation experiments with the primitive equations. Monthly Weather Review. 91, pp. 99-165.
- [21] Vaibar, R., 2008. CFD simulation of mixing phenomena in Pressurised Water in the presence of density gradients. PhD thesis, Technische Universität Dresden.
- [22] Vaibar, R., Da Silva, M. J., Sühnel, T., 2007. Buoyancy driven turbulent flow and experimental validation at the VeMix test facility. Applied and Computational Mechanics, 2007, pp. 677-684.
- [23] Winckelmans, G. S., Lund, T. S., Carati, D., Wray, A. A., 1996. A priori testing of subgrid scale models for the velocity-pressure and vorticity-velocity formulations. In: Proceedings of the Summer Program, Center of Turbulence Research, pp. 309-328.